APPLIED SCIENCES AND ENGINEERING

# De novo rational design of a freestanding, supercharged polypeptide, proton-conducting membrane

Chao Ma[1,2]*, Jingjin Dong[3]*, Marco Viviani[3]*, Isotta Tulini[3], Nicola Pontillo[2], Sourav Maity[4], Yu Zhou[2], Wouter H. Roos[4], Kai Liu[1,5†], Andreas Herrmann[2,6,7†], Giuseppe Portale[3†]



**Proton translocation enables important processes in nature and man-made technologies. However, controlling proton conduction and fabrication of devices exploiting biomaterials remains a challenge. Even more difficult is the design of protein-based bulk materials without any functional starting scaffold for further optimization. Here, we show the rational design of proton-conducting, protein materials exceeding reported proteinaceous systems. The carboxylic acid–rich structures were evolved step by step by exploring various sequences from intrinsically disordered coils over supercharged nanobarrels to hierarchically spider β sheet containing protein-supercharged polypeptide chimeras. The latter material is characterized by interconnected β sheet nanodomains decorated on their surface by carboxylic acid groups, forming self-supportive membranes and allowing for proton conduction in the hydrated state. The membranes showed an extraordinary proton conductivity of 18.5 ± 5 mS/cm at RH = 90%, one magnitude higher than other protein devices. This design paradigm offers great potential for bioprotonic device fabrication interfacing artificial and biological systems.**

## INTRODUCTION

In nature, ions and protons mediate signaling and flow of biological information (*1*). Proton conduction is responsible for many fundamental processes in biology, such as bioluminescence (*2*), adenosine 5′-triphosphate synthesis (*3*), and light-triggered proton translocation (*4*). On the other hand, proton conduction is widely of interest in materials science and energy applications such as sensors and fuel cells (*5*–*7*). Several synthetic materials exhibiting proton translocation behavior have been developed such as Nafion ionomer and (metal-)organic/inorganic hybrid systems (*8*–*11*). However, several features of these synthetic materials such as their fabrication in organic solvent, complicated functionalization, and little biocompatibility impede the interfacing with the fields of bioelectronics or biotechnology. Moreover, it represents a challenge to precisely adjust parameters such as molecular weight, charge density, or charge distribution of polymeric materials to control proton conduction.

The past decade witnessed the emergence of biomaterials dedicated to proton conduction, particularly involving existing scaffolds or sequences and exploiting their intrinsic proton-conducting behavior (*12*–*17*). Very recently, films made by proton-conducting protein nanowires able to continuously generate electric power in ambient environment were prepared (*18*). Yet, the rational de novo design of proton-conducting peptide materials making use of sequential design steps to increase proton conductivity in a successive manner remains elusive. In the hydrated state, it is well accepted that protons are transported via water molecules along an adjacent hydrogen bond network, a mechanism termed proton hopping (Grotthuss mechanism) (*19*). This hopping process can be further enhanced in films or other devices by introducing self-assembly at the nanoscale and domain association via tie chain interconnection (*20*–*24*). This knowledge can serve as a blueprint to design proton-conducting structures from scratch. In the context of protein design, great success has been achieved by evolving innovative catalysts with remarkable activities (*25*, *26*). One of the reasons for this success is that activities of enzymes can be screened effectively and are properties of isolated molecules. However, the generation of innovative protein bulk materials by protein design methods where superstructure formation and self-assembly processes of a large ensemble of biomacromolecules determine the final properties is still a great challenge.

Here, we present the stepwise evolution of a protein proton-conducting membranes. The starting point for this endeavor is a set of unfolded anionic supercharged polypeptides (SUPs) containing glutamic acid residues. These hydrophilic charged moieties serve as proton carriers and were incorporated into the polypeptide backbone at different charge densities. The proton-conducting performances of these unfolded systems with structural flexibility were assessed in comparison to a folded β barrel nanostructure with fixed glutamic/aspartic acid proton carriers on the protein surface. With the aim to obtain freestanding membranes and after exploring different possible solutions, the structural design was perfected by amalgamating silk-like β sheet structures with anionic SUPs to form self-assembled nanostructures with surfaces decorated by dense carboxylic acid groups, allowing for hydration, proton dissociation, and formation of proton conduction pathways. This evolutionary approach resulted in the production of a mechanically stable freestanding membrane with outstanding proton conductivity of 18.5 ± 5.5 mS/cm, which surpasses so far reported transport properties of protein-based systems by one order of magnitude.

## RESULTS AND DISCUSSION

The supercharged proteins used here are derived from elastin, a native component in connective tissues of vertebrates. By introduction of specific amino acid residues at the fourth position X of the

[1]State Key Laboratory of Rare Earth Resource Utilization, Changchun Institute of Applied Chemistry, Chinese Academy of Sciences, 130022 Changchun, China. [2]Polymer Chemistry and Bioengineering, Zernike Institute for Advanced Materials, Nijenborgh 4, 9747 AG Groningen, The Netherlands. [3]Macromolecular Chemistry and New Polymeric Materials, Zernike Institute for Advanced Materials, University of Groningen, Nijenborgh 4, 9747 AG, The Netherlands. [4]Molecular Biophysics, Zernike Institute for Advanced Materials, University of Groningen, Nijenborgh 4, 9747 AG Groningen, The Netherlands. [5]Department of Chemistry, Tsinghua University, 100084 Beijing, China. [6]DWI–Leibniz Institute for Interactive Materials, Forckenbeckstr. 50, 52056 Aachen, Germany. [7]Institute of Technical and Macromolecular Chemistry, RWTH Aachen University, Worringerweg 2, 52074 Aachen, Germany.
*These authors contributed equally to this work.
†Corresponding author. Email: kai.liu@ciac.ac.cn (K.L.); herrmann@dwi.rwth-aachen.de (A.H.); g.portale@rug.nl (G.P.)

$(GVGXG)_n$ repeat units and further functionalization, elastin-like polypeptides have been extensively exploited for protein engineering, biopolymer liquefaction, and the modification of interfaces (*27*–*29*). Glutamic acid (Glu or E), which can be easily deprotonated under physiological conditions and plays an important role in proton conductivity (*13*), was introduced into the X site of $(GVGXG)_n$ sequences, leading to unstructured negatively supercharged SUP-Es (Fig. 1A and fig. S1). The supercharged proteins here are defined accordingly to a class of engineered or naturally existing proteins with a high positive or negative net charge (typically >1 net charge unit per kDa molar mass) (*28*). These materials that, unlike many other proteins, do not show any secondary or tertiary structure represent the starting point for the systematic evolution of proton conductivity using a rational de novo designed protein scaffold. Here, three different variants bearing different charge densities were constructed via molecular cloning, resulting in the following three systems named as E72, HC_E35, and DC_E108. Typically, E72 indicates that there are 72 negative charges encoded in the disordered polypeptide chain. HC_E35, exhibiting 1 charge per 10 amino acid residues, contains 35 glutamic acids (half of E72) in the protein backbone and, at the same time, exhibits the same degree of polymerization as E72, thus termed half-charged E35. Using a similar abbreviation scheme, DC_E108 exhibits the double charge density of E72 (two charges in every five residues), and therefore, this variant is termed double-charged E108. Details about the cloning strategy and expression of the recombinant polypeptides are given in the Supplementary Materials. To test the protonic translocation efficiency, the samples were thoroughly purified by extensive dialysis, and thus, the resulting solutions exhibited pH values in the range of 4.0 to 5.5.

Electrochemical impedance spectroscopy (EIS) using gold interdigitated electrodes (IDEs) on a $SiO_2$/Si substrate was used for the evaluation of thin-film proton conduction. Alternating current was applied to the system and expressed as real/imaginary impedance in a Nyquist curve, wherein a semicircle resides in the high-frequency region and an inclined curve is obtained in the low-frequency part. Each SUP solution (50 μl, 5 mg/ml) was casted and evenly spread on the surface of the gold IDEs, followed by vertically hanging over to form a smooth and highly homogeneous SUP nanofilm (thickness, ~40 nm; Fig. 1B and figs. S3 and S4). Note that all the transport data obtained for the thin films and reported in the following are gathered on films with almost identical thickness (table S2). The proton transport was measured as a function of relative humidity (RH) (Fig. 1C). At RH = 50%, the E72 film showed an impedance value of about 5.5 megohm (Fig. 1C, i). At RH = 75%, the impedance became 2.5 megohm, showing enhanced but still weak proton conduction. When increasing the humidity to 90%, the resistance of the circuit was drastically reduced to 31 kilohm, implying a positive RH-dependent behavior of the proton translocation of the films (Fig. 1C, ii). This drastic ionic conductivity increase is due to the absorption of a large number of water molecules around the —COOH groups above RH > 70 to 80% with subsequent increase of the proton mobility, in agreement with the behavior of other protonic conducting devices (*12*, *13*) and in line with the film swelling results that will be discussed below.

Besides RH, another factor determining proton conductivity was investigated. It is known that proton conduction is related to charge carrier density (*30*). In the following, the effect of local charge densities was evaluated through comparing the resistance values of specimens HC_E35, E72, and DC_E108 at 90% RH. It was observed that HC_E35 with the lowest charge density gives the largest resistance (ca. 42 kilohm), indicating relatively low conductance (Fig. 1D). E72 with a doubled charge density showed a reduced resistance.

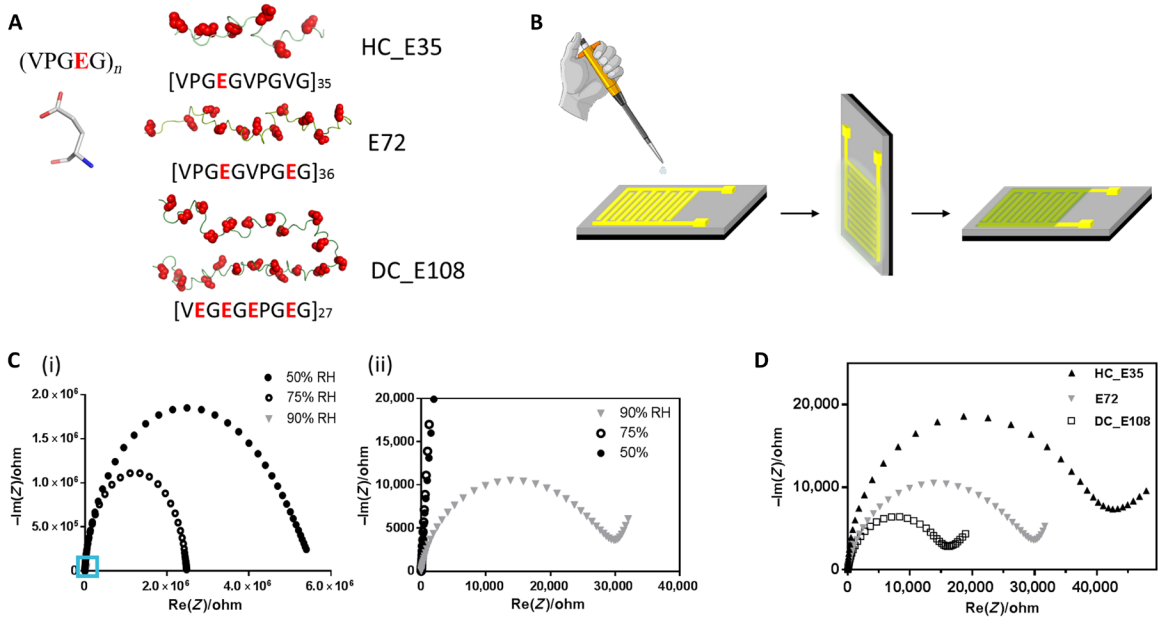


**Fig. 1. Structure of anionic SUP, devices for proton conductivity measurements and performance of different SUPs in these devices.** (**A**) Primary structure of SUPs engineered with various charge densities. (**B**) Fabrication protocol of protein films deposited on gold IDEs. (**C**) Impedance measurement of sample E72 in the shape of Nyquist plot under different RH. The figure (ii) is the zoom-in region of (i) indicated by the blue square. (**D**) Nyquist plot of protein thin films from samples E72, HC_E35, and DC_E108 equilibrated at RH = 90%. The extrapolated intercept of the observed semicircle with the *x* axis is indicative of the sample resistance that scales as HC_E35 > E72 > DC_E108.

The DC_E108 sample characterized by the highest charge density exhibited the lowest resistance in this series. Thus, by tuning the charge density of the disordered proteins, we successfully controlled proton conductance behavior of proteins within films on IDE. Notably, the whole set of devices did not show any sign of defects at the established conditions during the testing (24 hours at high RH), owing to high stability and uniformity of the thin films made from SUPs (fig. S4C).

Next, we extended our study to explore folded protein backbones. In synthetic ion-conducting polymers, the proton transport has been augmented by the introduction of nanostructures and phase separation (*31*, *32*). Thus, it is reasonable to investigate folded nanosized proteins. Therefore, a nanosized protein scaffold was equipped with carboxylic acids on the surface that, compared to SUPs, reside on fixed positions on the protein surface. As the protein, −30GFP (green fluorescent protein) was selected, which exhibits 30 negative charges (Asp and Glu) on the rim of a β barrel structure (Fig. 2A) (*33*). The negative charges were introduced by genetic mutation of positive amino acid residues and work as $H^+$ donors. Similar to SUPs, homogeneous thin films were prepared from −30GFP on IDEs. The resulting data represented in a Nyquist plot showed a resistance of 14 kilohm, noticeably lower than that of unstructured SUPs, E72 and HC_E35 (Fig. 2, B and C). The respective conductance can be calculated on the basis of the equation $\sigma = \frac{d}{\rho^* l^* (N-1)}$ (Eq. 1), where $d$ is the separation between two electrode fingers, $l$ is the length of an individual finger, and $N$ represents the total number of IDEs (Fig. 2C). X-ray diffraction can be used to investigate structural information inside the supercharged protein samples, providing distinct signatures for random coils and structured domains. As the samples are supported onto a substrate, grazing incidence x-ray diffraction (GIXD) measurements were carried out. In GIXD, monochromatic x-rays are incoming at an incident angle with respect to the substrate and are recorded by a two-dimensional (2D) detector after being diffracted by the thin films deposited on silicon substrates. The recorded GIXD patterns are then inspected for the presence of any diffraction signal. The GIXD patterns and the plots of the diffracted intensity distribution versus the vertical $q_z$ and the horizontal $q_y$ scattering vector for the E72 and −30GFP samples are presented in Fig. 2D and fig. S5. No specific diffraction signals were detected in the scattering through E72 films, confirming its intrinsically unstructured or random coil state. On the contrary, the scattering pattern for the −30GFP thin film shows two distinct diffraction signals located at $q \approx 0.65$ Å$^{-1}$ and $q \approx 0.18$ Å$^{-1}$, respectively. The recorded peaks correspond to real distances of about 9 and 35 Å, matching the characteristic dimensions of GFPs (*34*, *35*). Considering the nanoscopic dimension of the −30GFP β barrel (24 Å by 42 Å), the 35-Å spacing is closely related to the average interbarrel distance and suggests random (or very weak) local orientation of the barrels (*34*). Note that the charge density of −30GFP is −0.12, which is substantially smaller than that of E72 and DC_E108 (−0.18 and −0.35, respectively; table S1). Thus, our results infer that the nanostructured nature of the −30GFPs thin film observed by GIXD might facilitate the process of proton translocation. These results imply that by rational engineering of protein motifs and introduction of β sheet domains, the performance of proton conduction can be readily enhanced.

Motivated by the increase in proton conductivity due to displaying carboxylic acid units on a folded β barrel nanostructure, we combined these design elements with SUP structures. However, instead of relying on β barrels, we intended to exploit extended mechanically more stable β sheet structures. To not interfere with the β sheet formation, we placed the anionic SUPs as loops separating alternating β sheet units. As β sheet motif, we considered a sequence from spider silk, which additionally imparts excellent mechanical properties due to supramolecular structure formation (*36*, *37*). The design rationale of this chimeric protein is that the carboxyl residues are presented on the surface of the β sheet nanodomains and random coil chains connect those nanostructures. The specific mechanical characteristics of spider silk originate from β sheet nanocrystals

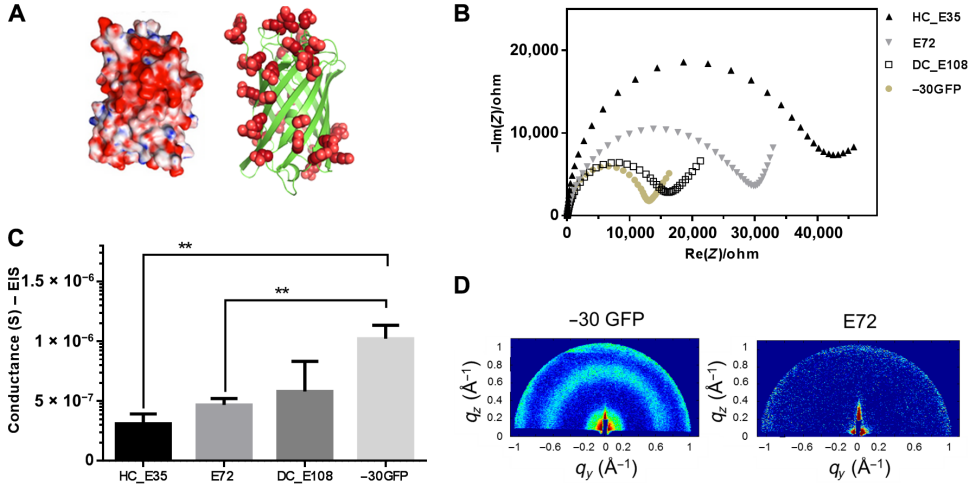


**Fig. 2. Supercharged −30GFP composed of a nanoscopic β barrel fold for proton conduction.** (**A**) 3D structure of supercharged −30GFP with excessive glutamic/aspartic acids (in red) on the protein surface. The left cartoon visualizes the structure in surface mode, showing positive residues in blue and negative ones in red. The right cartoon visualizes the −30GFP as a ribbon diagram exclusively presenting negative charges. (**B**) Impedance measurement of sample −30GFP (yellowish solid dots) in Nyquist plotting at 90% RH, compared with other SUP samples. (**C**) Comparison of conductance between samples E72, HC_E35, DC_E108, and −30GFP (**$P = 0.004$, $n > 3$). (**D**) GIXD patterns for structure investigation of the different films. Two distinct signals were observed for the nanostructured −30GFP (left), while no signal was detected for E72 films (right), indicating its unstructured nature.

consisting, to a large extend, of polyalanine (poly-A) sequences. The poly-A motifs form β sheet–rich interlocked hydrophobic regions due to strong intramolecular hydrogen bonding. These β sheet sequences were combined with the anionic SUP system, which we termed spider-E.

To synthesize this novel bioinspired material, we constructed a plasmid vector containing 18 repeats of a supercharged domain fused to a β strand–forming sequence. The building blocks of this chimeric protein include two components, i.e., the SUP part consisting of five elastin-like polypeptide units $(VPGEG)_5$ and the poly-A containing a part derived from spider silk (Fig. 3A). After expression and extensive dialysis (details are described in the Supplementary Materials), the recombinant anionic spider-E material was analyzed. Structure determination was first conducted by GIXD and Fourier transform infrared (FTIR) spectroscopy (Fig. 3, B and C). The GIXD data of a spider-E film prepared by drop-casting onto a Si substrate provide first evidence for the presence of the aimed β sheet nanostructures. The spider-E GIXD pattern shows two distinct reflections located at 1.2 and 0.46 nm, related to the intersheet spacing and interstrand distances occurring in the β sheet domains, respectively (Fig. 3B). The collected x-ray scattering pattern thus proves that highly compact and structured β sheet nanoassemblies were realized in the film. Despite a weak intensity modulation of the intersheet signal along the azimuthal direction, the full semiring nature of the diffraction signals in Fig. 3B indicates that the film has an isotropic structure, as a result of the solvent drop-casting method used here. From the width of the intersheet diffraction peak ($\Delta q_{intersheet}$), we estimated the average dimension of the β sheet nanodomains in the direction perpendicular to the sheet plane via the Debye-Scherrer formula ($D = 2\pi/\Delta q_{intersheet} \sim 20$ nm). Considering an intersheet distance of 1.2 nm, we estimated that approximately ~15 to 20 β sheets pile up together in one single nanocrystal domain. The measured intersheet distance of 1.2 nm is slightly larger than the one observed in other β sheet–rich proteins (*38*). This is most probably caused by the strong repulsion of the negative charges located in the loop regions of the β sheet nanocrystal structures, leading to an increase of the intersheet spacing. FTIR data further confirmed the GIXD observations. The amorphous E72 sample shows a characteristic amide I peak at 1640 $cm^{-1}$ in the FTIR spectra, indicating its random coil structure. After the incorporation of the poly-A motif, the amide I peak of spider-E shifts to 1620 $cm^{-1}$, indicating the existence of a typical β sheet structure (Fig. 3C). The formation of the β sheet nanocrystal structures was also confirmed by atomic force microscopy (AFM; see Fig. 3D) (*39*). AFM conducted on a supported film that was extensively exposed to liquid water to cause excessive swelling showed the presence of nano-objects with a height of ~3 nm and a

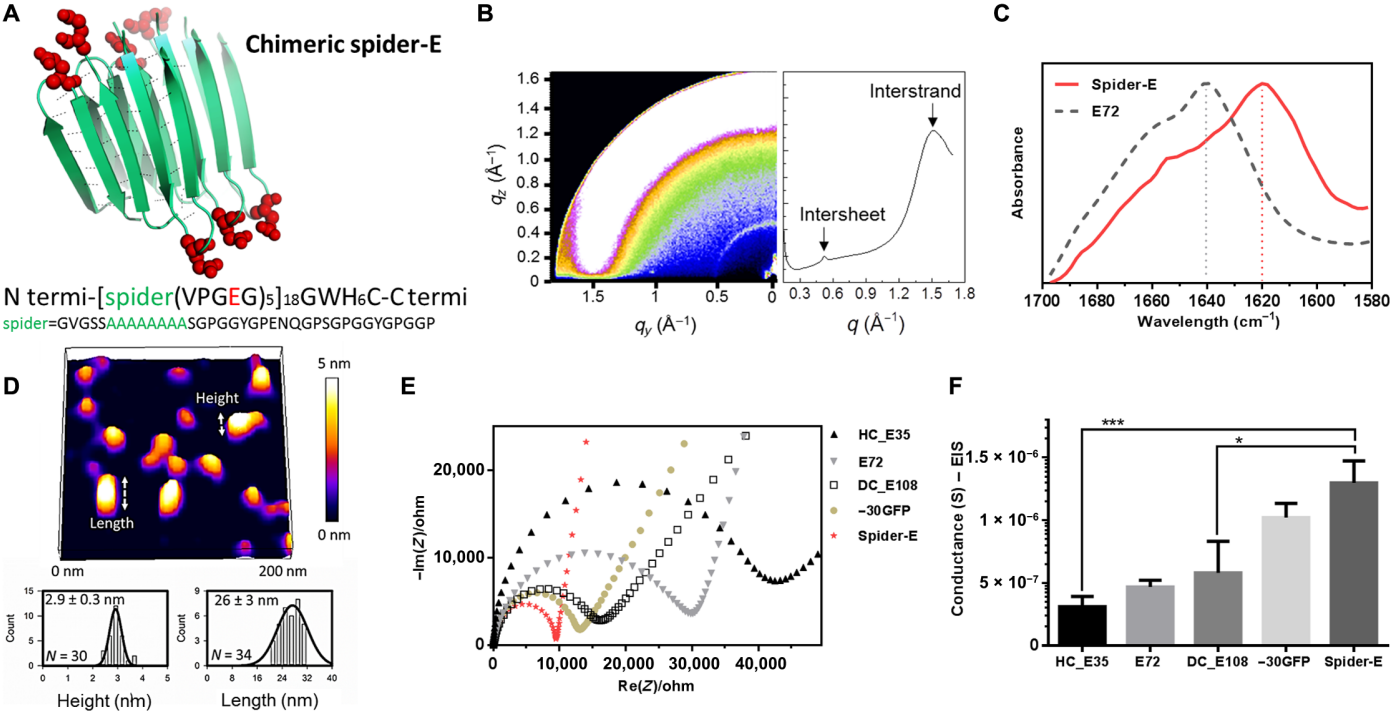


**Fig. 3. Sequence, structure, and proton conduction of recombinant supercharged spider-E thin films on IDE.** (**A**) Rationally designed supercharged spider silk–inspired proteins (spider-E). The spider motif contains a poly-A sequence (green) and anionic supercharged regions (red) that are forming the loops between the rigid β sheets. (**B**) Structure analyses of the spider-E supported film. Two peaks were detected by GIXD, indicating the characteristic intersheet and interstrand distances, respectively. (**C**) FTIR characterization of the films indicate random coils for the E72 sample (gray dashed line) with an amide I peak located at 1640 $cm^{-1}$ and a shift to a typical β sheet amide I peak for the spider-E sample (red solid line) at 1620 $cm^{-1}$. (**D**) Morphology analyses of the spider-E supported film. Quantification of the nanostructures assembled through spider β sheet domains by AFM. This sample was obtained by extensive swelling of the film by water contact to induce separation between the domains. (**E**) Nyquist plots obtained at RH = 90% for the five genetically engineered samples including spider-E. The impedance curve of the spider-E sample shows the lower resistance value among all the samples (red). (**F**) Comparison of conductance of the resulting devices demonstrating the stepwise increase in the transport properties due to the improved protein design. The proton transport of spider-E thin films on IDEs is noticeably higher than HC_E35 (***$P = 0.0009$, $n > 3$) and DC_E108 (*$P = 0.0155$, $n > 3$).

length of ~26 nm. Considering an expected tip convolution of a few nanometers at both sides, this length is in excellent agreement with the x-ray results discussed above. Furthermore, the measured height fits with the expected size of the β sheet strand reported (eight amino acids, ~2.8 nm; Fig. 3A). The proton transport of the novel bioinspired spider-E material in the hydrated state is displayed in Fig. 3 (E and F). The spider-E film exhibits a much higher proton conductance compared to amorphous SUPs films, confirming once more that the implementation of the nanostructure in the supercharged protein films is beneficial for the ionic transport. The peculiar design of the spider-E protein implies that, after self-assembly, the carboxylic hydrophilic groups are located on the surface of the β sheet nanodomains (Fig. 3A). Once hydrated, the proton movement thus occurs among the network of water molecules located in the nanoconfined space between the domains, with beneficial effect on the proton conduction (*5*). Absorption of water molecules inside the films can be measured by studying the swelling behavior of different systems as a function of various RH conditions (fig. S6). As expected, all the samples show large increase of the thickness for RH > 70 to 80%, suggesting the formation of a percolated water network that well correlates with the large increase in conductivity observed at the highest RH values. Further, the temperature dependence of the proton conductivity was investigated and compared for the SUP E72, the −30GFP, and the spider-E films (fig. S7). The conductivity change as a function of temperature followed the Arrhenius behavior for all the samples, and the calculated activation energies are in the range of 0.15 to 0.44 eV. These values are indicative for a Grotthuss-like conduction mechanism and are in agreement with values reported for other protein systems (*13*, *40*, *41*).

Owing to the introduction of the β sheet structures, the mechanical properties of the system improved, resulting in a freestanding membrane that can be readily produced. By drop-casting the spider-E solution on a hydrophobic surface (e.g., Teflon, to easily peel off the membrane), a transparent macroscopic membrane was fabricated with an approximate thickness of 3 μm and a diameter of 3.5 mm (Fig. 4A and fig. S8A). The membrane showed mechanical robustness with a yield strength of 38 ± 4 MPa, an elastic modulus of 216 ± 51 MPa, and an ultimate strain of 536 ± 56% (Fig. 4B and fig. S8, B and C). The data suggest the active integration of spider motifs into the bulk membrane and their positive role for building a robust material. The yield strength of our freestanding spider-E membrane is comparable to that of recombinant spider silk materials (fig. S8C). The ultimate strain of the spider-E membrane is much higher than other structural proteinaceous films most probably because of the contribution from the random-coil SUP motifs alternatingly introduced into the β sheet nanodomain networks. Following EIS analysis, the freestanding spider-E membrane exhibited an outstanding protonic conductivity of 18.5 ± 5 mS/cm at RH of 90% (Fig. 4C), which is one magnitude higher than reported for other protein systems (*13*, *14*). X-ray scattering data acquired in transmission geometry on this freestanding spider-E membrane confirmed the existence of β sheet nanodomains in agreement to what was observed for the supported film (fig. S8D). AFM analysis was further performed to inspect the membrane morphology (Fig. 4D). The AFM topographic image of the membrane surface at RH ~30% showed the presence of nanostructures with a strong tendency to aggregate (Fig. 4D, left). Exposing the membrane to RH ~90% triggers water absorption in between the β sheet nanodomains, and the assembled nanostructures become more visible (Fig. 4D, right). The dimensions of these nanostructures are in agreement with x-ray estimations reported above and the AFM observations presented in Fig. 3D. It is known that spider silk fibers are formed by self-assembled β sheets nanocrystals via an energetically favorable process and connected with random-coil tie chains (*42*). Thus, by combining the x-ray and AFM results, we can conclude that the spider motifs form β sheet nanosized domains that tend to stack together and have hydrophilic surfaces composed of the glutamic acid–rich SUP strands. This specific nanostructure and network formation probably facilitate exceptional proton hopping between adjacent $H_2O$ molecules in this class of materials (Fig. 4E).

Taking known protein sequences and using them in the same or in a different context as in nature to achieve bulk functionality is a reliable method to fabricate protein materials (*43*–*45*). Here, we went beyond that because we started from an anionically charged, nonnative sequence and evolved it further in a stepwise fashion by exploring different sequence contexts by protein engineering techniques. Besides pushing the limits of existing proteinaceous proton-conducting materials, this study represents one of the first examples that deals with the protein engineering and rational design of bulk functionality. It needs to be emphasized that besides improving mechanical properties, we successfully achieved the evolution of protein function that does not represent a property of an individual molecule but of a bulk architecture with collective properties originating from a molecular ensemble.

## CONCLUSIONS

In this study, we applied rational molecular de novo design and genetic engineering to achieve a bioinspired protein-derived bulk material with robust proton conduction properties and excellent mechanical stability. Multiple carboxylic acid–rich supercharged protein systems were characterized by biophysical tools including x-ray scattering, FTIR, and AFM, and their proton-conducting properties were studied using impedance spectroscopy. The design evolved from disordered random coils with different charge densities over folded supercharged GFP with a nanobarrel structure to chimeras of spider silk motifs fused to anionic SUPs, which form nano-to-meso superstructures. The latter architectures are characterized by extended β sheets that stack together to form interconnected nanodomains providing a mechanically stable membrane. The surfaces of these nanodomains contain anionic SUP moieties that, upon hydration, form percolated transport pathways for protons. The new-generation bioinspired bulk material obtained by exploring successive sequence designs shows a record value for protein-based device of 18.5 ± 5 mS/cm at RH = 90%. Our rational de novo design strategy opens up a new methodology to encode proteinaceous biomaterials with predetermined properties, holding great promise for biological and technical applications. Moreover, our approach not only allows the production of systems where the charge density can be readily tuned but also offers control over the precise location of the charged groups within the polymeric chains and the distance among them. The films of these materials are sensitive to humidity and might be further developed to biosensors recognizing more complicated analytes than water or might be even applied as $H^+$ transport membranes in miniaturized implantable biofuel cells of the future. In particular, the robust mechanical performance, the intrinsic biocompatibility, and the versatility of structural design of our proteinaceous materials make them suitable and sustainable for implantable devices.

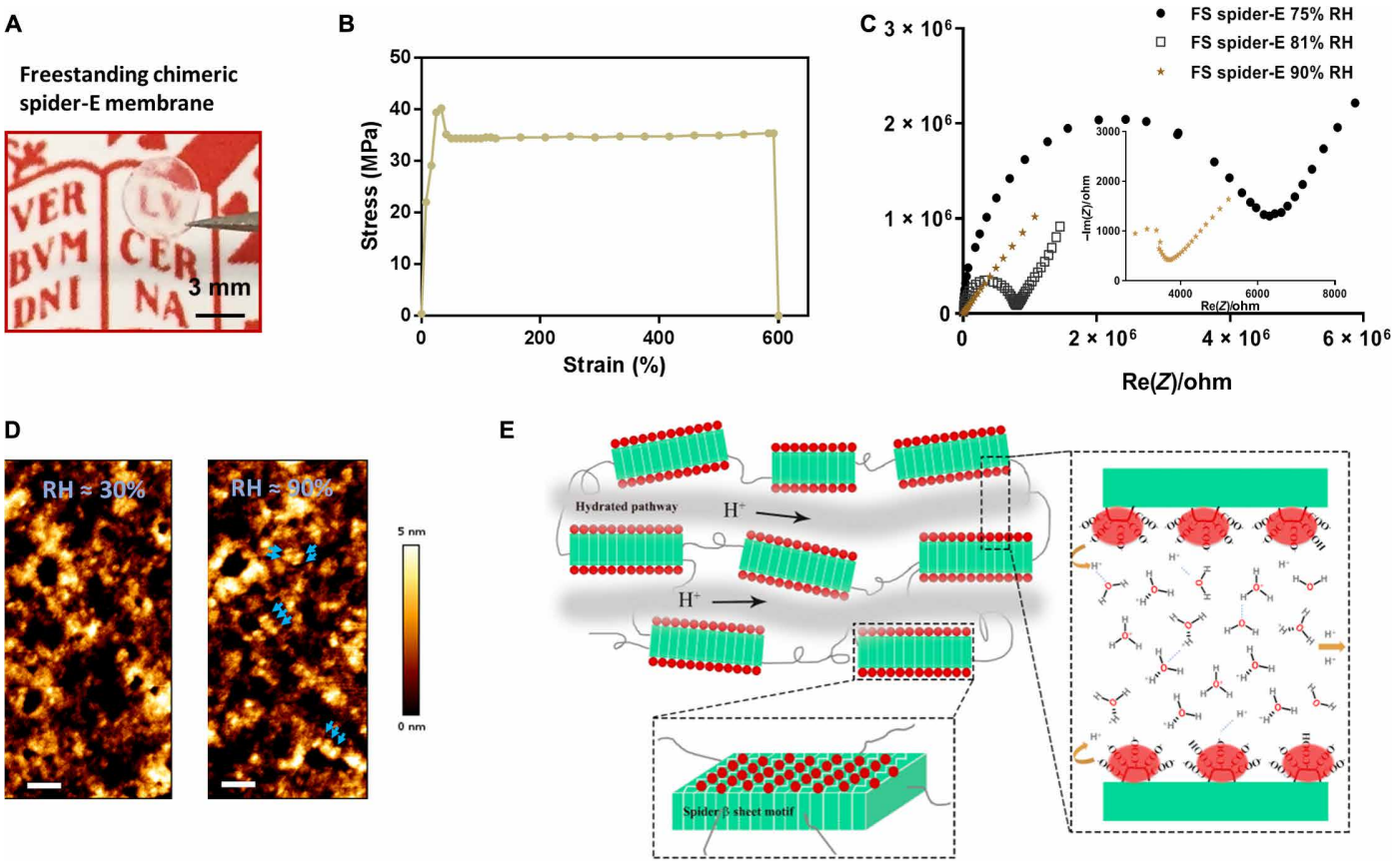


**Fig. 4. Bulk freestanding chimeric spider-E membrane with extraordinary proton transfer properties.** (**A**) A digital photograph illustrates the dimensions and transparency of the membrane. The protein membrane is clamped with a fine tweezer. Photo credit: Chao Ma, University of Groningen. (**B**) Mechanical characterization of the freestanding (FS) protein membrane, showing a typical tensile stretching curve. (**C**) Nyquist plot illustrating the conductance behavior of the FS spider-E membrane under different RHs. The film shows best proton translocation properties at 90% RH. (**D**) AFM characterization of the FS spider-E membrane under ~30 and ~90% RH conditions. Scale bars, 100 nm. Blue arrows point at distinguishable nanostructures. (**E**) Proposed mechanism of proton transport in the spider-E membrane at RH = 90%. The protons hop between water molecules nanoconfined in the hydrated network of nanodomains formed by spider β sheet motifs (in green). The glutamic acid residues in the chimeric nanostructures present carboxylic groups (in red) on the surface, providing the protons and coordinating water molecules.

## MATERIALS AND METHODS

### Materials

All chemicals were obtained from Sigma-Aldrich (The Netherlands and Germany). The water used in this research (typically 18.2 megohm·cm at 25°C) was from a Milli-Q ultrapure water system (Merck, Germany). Biochemicals for cloning and SUP expression, such as LB medium, salts, antibiotics, and inducer compounds, were used as received (from Sigma-Aldrich) without any further purification. The pUC19 cloning vector, restriction enzymes, and a GeneJET Plasmid Miniprep kit were purchased from Thermo Fisher Scientific (Waltham, MA). Digested DNA fragments were purified using QIAquick spin miniprep kits from QIAGEN (Valencia, CA). *Escherichia coli* XL1-Blue competent cells for plasmid amplification were purchased from Stratagene (La Jolla, CA). Oligonucleotides for sequencing were ordered from Sigma-Aldrich (St. Louis, MO). α-Cyano-4-hydroxycinnamic acid was used as matrix during matrix-assisted laser desorption/ionization (MALDI) mass spectrometry and was purchased from Thermo Fisher Scientific (Waltham, MA). Other chemicals and solvents used in the work are analytical grade.

### Molecular cloning and protein expression

Sequence details of three types of SUPs with different charge densities, namely, the half-, single-, and double-charged ones, are shown in fig. S1A and table S1. In general, recursive directional ligation was used for the plasmid construction. The monomers, including HC_E5, E9, and DC_E108, were treated with specific restriction enzymes for the oligomerization process. After three rounds of ligations, HC_E35, E72, and DC_E108 were obtained. For the folded protein −30GFP, we carried out mini-preps of the plasmid that was obtained from Addgene (#62936). The amplified vectors were verified by gene sequencing. The gene and amino acid sequence of −30GFP used in this study are listed in fig. S1B.

Using DNA cloning and gene oligomerization strategy, we successfully constructed the plasmids of spider-E hosting 18 repeats of the monomer, which is flanked with PflM I and Bgl I. The monomer gene consisting of one unit of the spider motif and of five (GVGEP) repeats (fig. S1C) was synthesized by IDP Company (The Netherlands). After four rounds of gene oligomerization with restriction enzymes PflM I and Bgl I, the whole sequence of spider-E was realized and

verified via enzymatic digestion and gene sequencing. The verification by nuclease digest was carried out using Nde I and EcoR I, as shown in fig. S2C with the gel and bands presented.

### Protein expression and purification

*E. coli* BLR(DE3) cells (Novagen) were transformed with the different expression vectors constructed above. For protein production, Terrific Broth (TB) medium (for 1 liter, 12 g of tryptone and 24 g of yeast extract) enriched with phosphate buffer (for 1 liter, 2.31 g of potassium phosphate monobasic and 12.54 g of potassium phosphate dibasic) and glycerol (4 ml per 1 liter of TB) and supplemented with ampicillin (100 μg/ml) was inoculated with an overnight starter culture to an initial optical density at 600 nm ($OD_{600}$) of 0.1 and incubated at 37°C with orbital agitation at 250 rpm until $OD_{600}$ reached 0.7. The production was induced by a temperature shift to 30°C. Cultures were then continued for additional 16 hours after induction. Cells were subsequently harvested by centrifugation (7000*g*, 30 min, 4°C), resuspended in lysis buffer [50 mM sodium phosphate buffer (pH 8.0), 300 mM NaCl, and 20 mM imidazole] to an $OD_{600}$ of 100, and disrupted with a constant cell disrupter (Constant Systems Ltd., Daventry, UK). Cell debris was removed by centrifugation (25,000*g*, 30 min, 4°C). Proteins of interest were purified from the supernatant under native conditions by Ni-Sepharose chromatography. Product-containing fractions were pooled and dialyzed against ultrapure water and then purified by anion exchange chromatography using a Q HP column [buffer A: 50 mM sodium phosphate and 50 mM NaCl (pH 7.4); buffer B: 50 mM sodium phosphate and 2 M NaCl (pH 7.4)]. The duration of elution process can be set as 20 column volumes. The product-containing fractions were dialyzed extensively against ultrapure water. Purified products were frozen in liquid nitrogen, lyophilized, and stored at −20°C until further use. Notably, all our proteins were collected in soluble form. No inclusion body or denaturation treatment was applied, which means that, exclusively, the supernatant of the lysate of expressed strains was used for sample purification. Compared to SUP and GFP samples, the purified amount of spider-E is relatively less. The reason is that spider-E has limited solubility majorly because of the hydrophobic β sheet domains. In the process of protein expression, a certain quantity of spider-E proteins formed inclusion bodies, leading to sediments after cell opening and centrifuge. To perform the experiments under ambient conditions, we exclusively collected the soluble spider-E in supernatant parts.

### SUP characterization

The concentrations of the purified products were determined by measuring absorbance at 280 nm using a spectrophotometer (SpectraMax M2, Molecular Devices, Sunnyvale, USA). Product purity was determined by SDS–polyacrylamide gel electrophoresis on 10% polyacrylamide gel. Afterward, gels were stained with Coomassie staining solution [40% methanol, 10% glacial acetic acid, and Brilliant Blue R-250 (1 g/liter)]. Photographs of the gels after staining were taken with a LAS-3000 Image Reader (Fuji Photo Film GmbH, Dusseldorf, Germany). The resulting stained gel is shown in fig. S2 (A and B). The supercharged proteins exhibit different electrophoretic mobility according to their charge and molecular weight ($M_w$). Some details on $M_w$ and sequences are shown in table S1.

Mass spectrometric analysis was performed using a 4800 MALDI-TOF Analyzer in linear positive mode. The polypeptide samples were mixed 1:1 (v/v) with α-cyano-4-hydroxycinnamic acid matrix (100 mg/ml in 70% acetonitrile and 0.1% trifluoroacetic acid). Mass spectra were analyzed with the Data Explorer version 4.9 (shown in fig. S2D). Values determined by mass spectrometry are in good agreement with the masses that were calculated on the basis of the amino acid sequence. The following masses were determined: HC_E35, 31.233 ± 50; E72, 36.505 ± 50; DC_E108, 30.469 ± 50; and −30GFP, 27.743 ± 50.

### Preparation and characterization of protein films drop-cast on electrodes

#### *Film preparation*

Drop-casting coating is the simplest technique for applying thin films to solid flat substrates. Sample solution is dropped on the substrate, and solvent spontaneously evaporates. Film thickness depends on the volume of solution used and on the solute concentration, both of which can be easily customized. There are also other variables that may affect the film structure such as how well the solvent wets the substrate, evaporation rate, capillary forces associated with drying, etc. In general, it is desirable to use solvents that are volatile, wet the substrate, and do not induce film detaching.

The film preparation protocol is as follows (fig. S3A):

1) Polypeptide and protein solutions were prepared by adding fresh Milli-Q water (resistivity, 18.2 megohm·cm) to in-stock lyophilized samples at −20°C. Before use, every solution was centrifuged at 13.2 relative centrifugal force for 3 min. Fifty microliters of solution with a concentration of 5 mg/ml was drop-cast on the top of an IDE (pretreated by ultraviolet/$O_3$ with wavelengths of 185 and 254 nm for 10 min) with a micropipette and spread evenly to cover all the 10 fingers of the electrode, avoiding touching the substrate or the electrodes with the pipette tip.

2) The wet covered IDE was then immediately placed in a closed Petri dish with wet (pure water) cotton on the side to let the solvent evaporate very slowly.

3) After waiting 1 to 2 hours, the electrode was lifted up with tweezers and placed vertically. The excess solution was accumulated at the edge (containing water and protein nonhydrostatically adsorbed) of the substrate and was removed with a tissue pressed gently at the edge of the wafer.

4) Wet layers took around 10 min to dry completely in air, and the produced thin films appear very homogeneous in thickness. At least three independent films of each solution were produced using the described method and tested for proton conductivity to obtain statistically meaningful data.

The thickness of each film was measured by cross-sectional scanning electron microscopy (fig. S3B) and AFM (fig. S3C). Furthermore, nebulization tests were performed to verify the stability of cast thin films on IDEs (fig. S4A).

#### *Atomic force microscopy*

AFM was used in this research to visualize the film surface structure (Figs. 3D and 4D) and to calculate the film thickness (fig. S3C). AFM imaging of the film surface topography was performed using a JPK ULTRA Speed AFM. Qp-bio (CB1) cantilevers with a nominal spring constant of 0.3 N/m and a nominal resonance frequency of 90 kHz were used for imaging both in liquid (Fig. 3D) and in air (Fig. 4D). The thin films were deposited on plasma-cleaned silicon surface using the same protocol used to prepare the film for the ionic conductivity measurements. The images were acquired in quantitative imagine ($QI^{TM}$) mode using minimal imaging force (<300 pN in air and <100 pN in liquid). Images were analyzed using the JPK data processing software.

AFM imaging to determine the film thickness was performed with an AFM instrument from Veeco, equipped with a phosphorus-doped Si cantilever with a resonance frequency of 267 to 294 kHz and a spring constant of 20 to 80 N/m. The surface of the thin film was scratched on the outside of the interdigitating gold finger area with a needle (0.4 mm by 20 mm) and then analyzed using AFM in tapping mode to measure the thickness of thin films (fig. S3C). A scan size of about 50 μm and a tip speed of 0.477 Hz were applied to obtain profile images. Several acquisitions from different scratches were taken. The data were analyzed with WSxM 5.0 Develop 8.3 software using an offset flattening function. At least 100 profiles were analyzed to calculate the average of the thickness of the films. The height profile corresponding to the white dashed line in the AFM images are displayed below the image, with the blue crosses indicating the position of the blue dashed lines in the profile image. A general overview of the determined heights of the customized protein thin films is presented in table S2.

### *EIS and cyclic voltammetry*

EIS measurements were used to measure the sample resistance and study the proton conductivity in the protein-based films. EIS measurements were performed using an SP-300 Biologic impedance spectrometer. The oscillating amplitude was fixed at 100 mV, and impedance spectra were collected by scanning the frequency from 7 MHz to 100 mHz in the logarithmic scale, with 10 points per decade on five replicas. The samples were placed in a humidified chamber where the RH could be adjusted in the range of 30 to 90% and the temperature set between 25° and 70°C. The impedance data were fitted using the EC-Lab Zfit software and a five-element equivalent circuit, typically used for thin polymer films deposited on gold IDEs.

At every RH, cyclic voltammetry (CV) experiments were run to know whether the device response is pseudo-linear and to exclude the presence of any redox process. The CV measurements were performed using an SP-300 Biologic impedance spectrometer by scanning a range from −1.5 to 1.5 V with a scan rate of 100 mV/s and 20 number of replicas. The acquired CV curves show no evidence of clear reduction or oxidation peaks in the scanned wide potential window (see fig. S4B).

It is necessary to consider the possibility that the films might swell and detach from the electrodes when high RH is applied. If the protein thin film is detached from the electrode, then the shape and the conductance of the EIS curve shall be immediately affected. Thus, a test by measuring the EIS response of an E72 thin film prior and after nebulization of water directly sprayed on the film surface was conducted. The water was nebulized at a distance of about 30 cm through the aid of a nebulizer connected to a pure water supply. Results are shown in fig. S4 (A and B). The system is completely reversible even after nebulization of water on top of the surface, and this is a further proof that the SUP thin films are electrostatically adsorbed on the substrate surface and do not detach from the electrode even after direct water contact. Note that the activity measured with nebulized water used in this test is higher than the one when applying a vapor phase used in the RH measurements. Thus, any issue regarding solubilization and removal of the films from the IDEs can be excluded.

### *Grazing incidence x-ray diffraction*

GIXD was used to characterize the structure of the polypeptide- and protein-based films. X-ray scattering provides a rational method to observe the existence of structure at the nanoscale. GIXD measurements were performed at the MINA instrument in Groningen. The instrument is built on a high-brilliance Cu rotating anode (x-ray wavelength $\lambda = 0.15413$ nm). Incoming x-rays impinge on the supported films with an incident angle of $\alpha_i = 0.2°$ with respect to the substrate plane and are collected using 2D detectors. A VÅNTEC-500 Bruker detector with a pixel size of 136 μm × 136 μm was used and placed 24 cm away from the sample. The beam center position on the GIXD pattern and the angular range were calibrated using a standard silver behenate powder sample. The GIXD patterns and data are plotted as a function of the horizontal $q_y$ and vertical $q_z$ scattering vectors

$$q_y = \frac{2\pi}{\lambda}(\sin(2\theta_f)\cos(\alpha_f))$$

$$q_z = \frac{2\pi}{\lambda}(\sin(\alpha_i)+\sin(\alpha_f))$$

where $2\theta_f$ is the scattering angle in the horizontal direction and $\alpha_f$ is the exit angle in the vertical direction. Data were all analyzed using a home-made MATLAB-based code.

The structure of the freestanding spider-E membrane was investigated using small-angle x-ray scattering (SAXS) in a transmission geometry (membrane perpendicular to the x-ray beam). The same instrument described above for the GIXD measurements was used. In this case, the circularly integrated SAXS profiles are reported as a function of the modulus of the isotropic scattering vector $q = 4\pi\sin(\theta)/\lambda$.

## SUPPLEMENTARY MATERIALS

Supplementary material for this article is available at http://advances.sciencemag.org/cgi/content/full/6/29/eabc0810/DC1

## REFERENCES AND NOTES


1. N. A. Kotov, J. O. Winter, I. P. Clements, E. Jan, B. P. Timko, S. Campidelli, S. Pathak, A. Mazzatenta, C. M. Lieber, M. Prato, R. V. Bellamkonda, G. A. Silva, N. W. S. Kam, F. Patolsky, L. Ballerini, Nanomaterials for neural interfaces. *Adv. Mater.* **21**, 3970–4004 (2009).
2. M. Valiadi, D. Iglesias-Rodriguez, Understanding bioluminescence in dinoflagellates—How far have we come? *Microorganisms* **1**, 3–25 (2013).
3. I. N. Watt, M. G. Montgomery, M. J. Runswick, A. G. Leslie, J. E. Walker, Bioenergetic cost of making an adenosine triphosphate molecule in animal mitochondria. *Proc. Natl. Acad. Sci. U.S.A.* **107**, 16823–16827 (2010).
4. Y. Sudo, A. Okazaki, H. Ono, J. Yagasaki, S. Sugo, M. Kamiya, L. Reissig, K. Inoue, K. Ihara, H. Kandori, S. Takagi, S. Hayashi, A blue-shifted light-driven proton pump for neural silencing. *J. Biol. Chem.* **288**, 20624–20632 (2013).
5. E. B. Trigg, T. W. Gaines, M. Maréchal, D. E. Moed, P. Rannou, K. B. Wagener, M. J. Stevens, K. I. Winey, Self-assembled highly ordered acid layers in precisely sulfonated polyethylene produce efficient proton transport. *Nat. Mater.* **17**, 725–731 (2018).
6. K.-D. Kreuer, G. Portale, A critical revision of the nano-morphology of proton conducting ionomers and polyelectrolytes for fuel cell applications. *Adv. Funct. Mater.* **23**, 5390–5397 (2013).
7. J. Molina, J. J. de Pablo, J. P. Hernández-Ortiz, Structure and proton conduction in sulfonated poly(ether ether ketone) semi-permeable membranes: A multi-scale computational approach. *Phys. Chem. Chem. Phys.* **21**, 9362–9375 (2019).
8. S. S. Nagarkar, S. M. Unni, A. Sharma, S. Kurungot, S. K. Ghosh, Two-in-one: Inherent anhydrous and water-assisted high proton conduction in a 3D metal-organic framework. *Angew. Chem.* **126**, 2676–2680 (2014).
9. M. R. Karim, K. Hatakeyama, T. Matsui, H. Takehira, T. Taniguchi, M. Koinuma, Y. Matsumoto, T. Akutagawa, T. Nakamura, S.-i. Noro, T. Yamada, H. Kitagawa, S. Hayami, Graphene oxide nanosheet with high proton conductivity. *J. Am. Chem. Soc.* **135**, 8097–8100 (2013).
10. J. A. Hurd, R. Vaidhyanathan, V. Thangadurai, C. I. Ratcliffe, I. L. Moudrakovski, G. K. H. Shimizu, Anhydrous proton conduction at 150 °C in a crystalline metal–organic framework. *Nat. Chem.* **1**, 705–710 (2009).
11. R. Fan, S. Huh, R. Yan, J. Arnold, P. Yang, Gated proton transport in aligned mesoporous silica films. *Nat. Mater.* **7**, 303–307 (2008).

12. C. Zhong, Y. Deng, A. F. Roudsari, A. Kapetanovic, M. P. Anantram, M. Rolandi, A polysaccharide bioprotonic field-effect transistor. *Nat. Commun.* **2**, 476 (2011).
13. D. D. Ordinario, L. Phan, W. G. Walkup IV, J.-M. Jocson, E. Karshalev, N. Hüsken, A. A. Gorodetsky, Bulk protonic conductivity in a cephalopod structural protein. *Nat. Chem.* **6**, 596–602 (2014).
14. N. Amdursky, X. Wang, P. Meredith, D. D. C. Bradley, M. M. Stevens, Long-range proton conduction across free-standing serum albumin mats. *Adv. Mater.* **28**, 2692–2698 (2016).
15. Y. Guo, Z. Jiang, W. Ying, L. Chen, Y. Liu, X. Wang, Z.-J. Jiang, B. Chen, X. Peng, A DNA-threaded ZIF-8 membrane with high proton conductivity and low methanol permeability. *Adv. Mater.* **30**, 1705155 (2017).
16. A. Pena-Francesch, H. Jung, M. A. Hickner, M. Tyagi, B. D. Allen, M. C. Demirel, Programmable proton conduction in stretchable and self-healing proteins. *Chem. Mater.* **30**, 898–905 (2018).
17. X. Strakosas, J. Selberg, Z. Hemmatian, M. Rolandi, Taking electrons out of bioelectronics: From bioprotonic transistors to ion channels. *Adv. Sci.* **4**, 1600527 (2017).
18. X. Liu, H. Gao, J. E. Ward, X. Liu, B. Yin, T. Fu, J. Chen, D. R. Lovley, J. Yao, Power generation from ambient humidity using protein nanowires. *Nature* **578**, 550–554 (2020).
19. N. Agmon, The Grotthuss mechanism. *Chem. Phys. Lett.* **244**, 456–462 (1995).
20. K. L. Naughton, L. Phan, E. M. Leung, R. Kautz, Q. Lin, Y. Van Dyke, B. Marmiroli, B. Sartori, A. Arvai, S. Li, M. E. Pique, M. Naeim, J. P. Kerr, M. J. Aquino, V. A. Roberts, E. D. Getzoff, C. Zhu, S. Bernstorff, A. A. Gorodetsky, Self-assembly of the cephalopod protein reflectin. *Adv. Mater.* **28**, 8405–8412 (2016).
21. J. Lerner Yardeni, M. Amit, G. Ashkenasy, N. Ashkenasy, Sequence dependent proton conduction in self-assembled peptide nanostructures. *Nanoscale* **8**, 2358–2366 (2016).
22. O. Kim, K. Kim, U. H. Choi, M. J. Park, Tuning anhydrous proton conduction in single-ion polymers by crystalline ion channels. *Nat. Commun.* **9**, 5029 (2018).
23. P. Ramaswamy, R. Matsuda, W. Kosaka, G. Akiyama, H. J. Jeon, S. Kitagawa, Highly proton conductive nanoporous coordination polymers with sulfonic acid groups on the pore surface. *Chem. Commun.* **50**, 1144–1146 (2014).
24. A. Pena-Francesch, M. C. Demirel, Squid-inspired tandem repeat proteins: Functional fibers and films. *Front. Chem.* **7**, 69 (2019).
25. S. Studer, D. A. Hansen, Z. L. Pianowski, P. R. E. Mittl, A. Debon, S. L. Guffy, B. S. Der, B. Kuhlman, D. Hilvert, Evolution of a highly active and enantiospecific metalloenzyme from short peptides. *Science* **362**, 1285 (2018).
26. C. Zeymer, D. Hilvert, Directed evolution of protein catalysts. *Annu. Rev. Biochem.* **87**, 131–157 (2018).
27. J. R. Simon, N. J. Carroll, M. Rubinstein, A. Chilkoti, G. P. López, Programming molecular self-assembly of intrinsically disordered proteins containing sequences of low complexity. *Nat. Chem.* **9**, 509–515 (2017).
28. C. Ma, A. Malessa, A. J. Boersma, K. Liu, A. Herrmann, Supercharged proteins and polypeptides. *Adv. Mater.* , 1905309 (2020).
29. C. Ma, J. Su, B. Li, A. Herrmann, H. Zhang, K. Liu, Solvent-free plasticity and programmable mechanical behaviors of engineered proteins. *Adv. Mater.* **32**, e1907697 (2020).
30. Y. Daiko, K. Katagiri, A. Matsuda, Proton conduction in thickness-controlled ultrathin polycation/nafion multilayers prepared via layer-by-layer assembly. *Chem. Mater.* **20**, 6405–6409 (2008).
31. C. Yin, J. Li, Y. Zhou, H. Zhang, P. Fang, C. He, Phase separation and development of proton transport pathways in metal oxide nanoparticle/nafion composite membranes during water uptake. *J. Phys. Chem. C* **122**, 9710–9717 (2018).
32. A. Onuma, J. Kawaji, M. Morishima, T. Mizukami, Y. Takamori, K. Yamaga, Effects of micro-phase-separated structures on proton conductivity and methanol permeability in polymer electrolyte membranes. *Polymer* **55**, 2673–2677 (2014).
33. M. S. Lawrence, K. J. Phillips, D. R. Liu, Supercharging proteins can impart unusual resilience. *J. Am. Chem. Soc.* **129**, 10110–10112 (2007).
34. J. Dou, A. A. Vorobieva, W. Sheffler, L. A. Doyle, H. Park, M. J. Bick, B. Mao, G. W. Foight, M. Y. Lee, L. A. Gagnon, L. Carter, B. Sankaran, S. Ovchinnikov, E. Marcos, P.-S. Huang, J. C. Vaughan, B. L. Stoddard, D. Baker, De novo design of a fluorescence-activating β-barrel. *Nature* **561**, 485–491 (2018).
35. F. Rico, A. Rigato, L. Picas, S. Scheuring, Mechanics of proteins with a focus on atomic force microscopy. *J. Nanobiotechnology* **11** Suppl 1, S3 (2013).
36. E. L. Morley, D. Robert, Electric fields elicit ballooning in spiders. *Curr. Biol.* **28**, 2324–2330. e2 (2018).
37. Q. Wang, H. C. Schniepp, Strength of recluse spider's silk originates from nanofibrils. *ACS Macro Lett.* **7**, 1364–1370 (2018).
38. S. J. Roeters, A. Iyer, G. Pletikapić, V. Kogan, V. Subramaniam, S. Woutersen, Evidence for intramolecular antiparallel beta-sheet structure in alpha-synuclein fibrils from a combination of two-dimensional infrared spectroscopy and atomic force microscopy. *Sci. Rep.* **7**, 41051 (2017).
39. M. C. Piontek, W. H. Roos, Atomic force microscopy: An introduction, in *Single Molecule Analysis: Methods and Protocols,* E. J. G. Peterman, Ed. (Springer, 2018), pp. 243–258.
40. C. A. Wraight, Chance and design—Proton transfer in water, channels and bioenergetic proteins. *Biochim. Biophys. Acta* **1757**, 886–912 (2006).
41. S. Cukierman, Et tu, Grotthuss! and other unfinished stories. *Biochim. Biophys. Acta* **1757**, 876–885 (2006).
42. N. A. Oktaviani, A. Matsugami, A. D. Malay, F. Hayashi, D. L. Kaplan, K. Numata, Conformation and dynamics of soluble repetitive domain elucidates the initial β-sheet formation of spider silk. *Nat. Commun.* **9**, 2121 (2018).
43. Y. Wang, P. Katyal, J. K. Montclare, Protein-engineered functional materials. *Adv. Healthc. Mater.* **8**, e1801374 (2019).
44. X. Hu, P. Cebe, A. S. Weiss, F. Omenetto, D. L. Kaplan, Protein-based composite materials. *Mater. Today* **15**, 208–215 (2012).
45. N. A. Carter, T. Z. Grove, Functional protein materials: Beyond elastomeric and structural proteins. *Polym. Chem.* **10**, 2952–2959 (2019).
46. R. V. Lewis, Spider silk: Ancient ideas for new biomaterials. *Chem. Rev.* **106**, 3762–3774 (2006).
47. J. G. Hardy, A. Leal-Egaña, T. R. Scheibel, Engineered spider silk protein-based composites for drug delivery. *Macromol. Biosci.* **13**, 1431–1437 (2013).
48. C. L. Tucker, J. A. Jones, H. N. Bringhurst, C. G. Copeland, J. B. Addison, W. S. Weber, Q. Mou, J. L. Yarger, R. V. Lewis, Mechanical and physical properties of recombinant spider silk films using organic and aqueous solvents. *Biomacromolecules* **15**, 3158–3170 (2014).



**Acknowledgments**

**Funding:** This research was supported by the European Research Council (ERC Advanced Grant SUPRABIOTICS, grant no. 694610), the Zernike Institute for Advanced Materials, the Chinese Academy of Sciences President's International Fellowship Initiative (grant no. 2018VBA0008), the Scientific Instrument Developing Project of the Chinese Academy of Sciences (grant no. ZDKYYQ20180001), and the National Natural Science Foundation of China (grant nos. 21704099, 21877104, 21834007, and 21801235). **Author contributions:** G.P., A.H., and C.M. designed research. C.M., I.T., M.V., N.P., J.D., S.M., Y.Z., and K.L. performed research. C.M., J.D., M.V., S.M., W.H.R., and G.P. analyzed the data. A.H., C.M., and G.P. conceived and wrote the manuscript. All the authors have read and approved the manuscript before submission. **Competing interests:** The authors declare that they have no competing interests. **Data and materials availability:** All data needed to evaluate the conclusions in the paper are present in the paper and/or the Supplementary Materials. Additional data related to this paper may be requested from the authors.

Submitted 7 April 2020
Accepted 4 June 2020
Published 17 July 2020
10.1126/sciadv.abc0810

**Citation:** C. Ma, J. Dong, M. Viviani, I. Tulini, N. Pontillo, S. Maity, Y. Zhou, W. H. Roos, K. Liu, A. Herrmann, G. Portale, De novo rational design of a freestanding, supercharged polypeptide, proton-conducting membrane. *Sci. Adv.* **6**, eabc0810 (2020).